Enhanced THz emission from spintronic Fe/Pt emitters through crystal growth optimization

Agne Ciuciulkaite,[1, a)] Oliver Gueckstock,[2, 3] Anna Ravensburg,[1] Merlin Pohlit,[1] Tobias Warnatz,[1] Tobias Kampfrath,[2, 3] Georg Schmidt,[4] Evangelos Th. Papaioannou,[4, b)] and Vassilios Kapaklis[1, c)]

[1)]*Department of Physics and Astronomy, Uppsala University, Box 516, SE-75120 Uppsala, Sweden*

[2)]*Department of Physics, Freie Universität Berlin, Arnimallee 14, 14195 Berlin, Germany*

[3)]*Department of Physical Chemistry, Fritz Haber Institute, Faradayweg 4-6, 14195 Berlin, Germany*

[4)]*Institut für Physik, Martin-Luther-Universität Halle-Wittenberg, Von-Danckelmann-Platz 2, 06120 Halle, Germany*

We investigate the THz emission characteristics of ferromagnetic/non-magnetic metallic heterostructures, focusing on thin Fe/Pt bilayers. In particular, we report on the impact of optimized crystal growth of the epitaxial Fe layers on the THz emission amplitude and spectral bandwidth. We demonstrate an enhancement of the emitted intensity along with an expansion of the emission bandwidth. Both are related to reduced spin scattering and higher interface transmission. Our work provides a pathway for devicing optimal spintronic THz emitters based on epitaxial Fe. It also highlights how THz emission measurements can be utilized to characterize the changes in out-of-equilibrium spin current dynamics in metallic heterostructures, driven by subtle structural refinement.

Electromagnetic THz radiation covers a broad bandwidth of the electromagnetic spectrum from 100 GHz to 30 THz[1], that lies between the microwave and the far infrared band. A range of scientific and industrial communities are utilizing THz radiation, spanning from chemistry and material sciences to medicine and security[2]. Furthermore, THz spectroscopy offers new possibilities to investigate deeper the solid state since the magnon and phonon excitations can typically be found in the range of THz frequencies, corresponding to femtoseconds in the time domain[3,4]. Commonly THz generation is based on optical rectification effects in non-linear crystals and on photocurrents in semiconcductors after excitation from femtosecond laser pulses. Recent developments in spintronics have demonstrated the first usage of ultrafast spin-related phenomena for THz emission[5] that has the potential to revolutionize the THz field and its applications[6].

The physical mechanism of the generation of THz radiation in spintronic THz emitters is based on the inverse spin Hall effect (ISHE)[7]. When heterostructures consisting of ferromagnetic (FM) and non-magnetic (NM), usually heavy metals (HM) thin layers, are illuminated by ultrafast femtosecond (fs) laser pulses, spin polarized electrons in the magnetized FM layer are excited and form a superdiffusive spin current that enters into the NM-later. The ISHE converts this longitudinal spin-polarized charge current into a transient transverse charge current in the NM layer, resulting in THz emission.[3,5,8,9]. So far the scientific challenge of engineering the THz emission, has been addressed in various ways: different material compositions of FM/NM systems with a variety of layer thicknesses[5,9–12], ferri- and antiferromagnetic metal/Pt structures[13–15], spintronic emitters assisted by a metal-dielectric photonic crystal[16], metallic trilayer structures with different patterned structures[17], interface

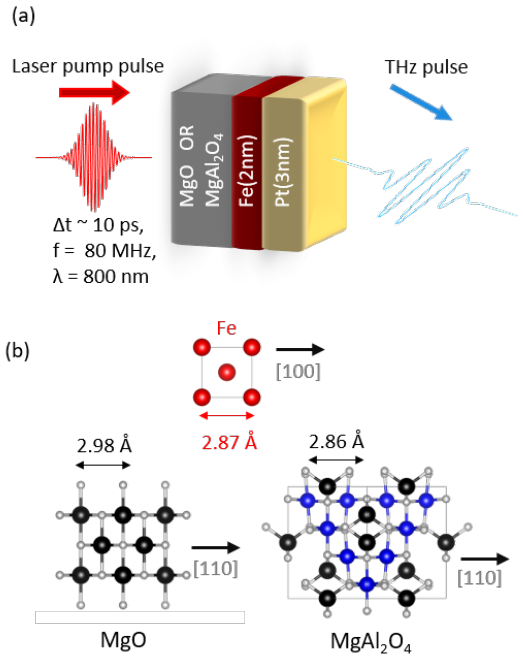

Figure 1. Schematics of (a) THz emission from FM/NM Fe/Pt bilayers and (b) lattice structure of crystalline Fe, MgO and $MgAl_2O_4$. The directions of substrates indicate the in-plane direction and lattice site spacing for the Fe growth. Fe grows rotated by 45 °with respect to the MgO or $MgAl_2O_4$ lattice, that is, along the [110] direction.

materials and substrates[8,18–21] and THz emission using different excitation wavelengths[22–24]. In this work we focus on the ferromagnetic layer (Fe), which is the source of the spin current. We show that by structural engineering the Fe layer we can alter the intrinsic properties of the spin current pulse in to the NM layer and thus modify the emitted THz amplitude and bandwidth. Recent studies in this direction by Nenno *et al.* [8] have revealed how the propagation of a spin current and sub-

[a)]Electronic mail: agne.ciuciulkaite@physics.uu.se
[b)]Electronic mail: evangelos.papaioannou@physik.uni-halle.de
[c)]Electronic mail: vassilios.kapaklis@physics.uu.se

sequently the THz emission are influenced by scattering processes and the density of structural defects in the multilayer stack. The parameter of elastic electron scattering lifetime was used to parametrize the overall defect density[8]. In an analogy to the dependence of photocurrents and THz emission on defect density in semiconducting materials[25], the defect engineering through the proper choice of substrates, promoting epitaxial FM layers, as well as through modification of the Fe-Pt interface quality, altered dramatically the emitted THz characteristics[8].

In this letter we turn our attention to the crystal quality of the FM layers, and investigate how it varies for the case of thin bcc Fe layers, deposited onto MgO and $MgAl_2O_4$ substrates. We proceed to investigate how this variation affects the THz emission from Fe/Pt bilayers. To this end, we fabricated and use Fe(20 Å)/Pt(30 Å) bilayers, which have experimentally been shown to result in the maximum amplitude of THz emission in comparison to other Fe/Pt thickness combinations according to Torosyan *et al.*[9].

Magnesium oxide is the most common substrate for the deposition of crystalline bcc Fe, since its crystal structure can match closely that of Fe. Along the [100] crystal direction the MgO lattice constant is 4.2 Å, but during the deposition, Fe grows with its lattice rotated 45 degrees in-plane with respect to the the MgO lattice plane, i.e. it grows along MgO [110] direction, along which the MgO lattice constant is 2.98 Å. Therefore, the MgO lattice constant is only 3.83 % larger than that of the Fe unit cell parameter, 2.87 Å (See Fig. 1(b)). Due to this low lattice mismatch, the growth of single crystalline layers is possible. Another promising candidate for the deposition of single crystalline Fe are the MgAl spinel crystals, with the chemical formula of $MgAl_2O_4$. Its crystal structure is based on that of diamond[26] where Mg atoms occupy almost the same positions as C atoms in diamond and have a lattice constant of 8.08 Å along the [100] direction[27–29]. Upon deposition, Fe atoms occupy the sites along [110] direction, and if we consider the cube-in-cube structure of the $MgAl_2O_4$ substrate, the lattice constant becomes 2.86 Å (See Fig. 1(b))[30]. Therefore, due to almost identical unit cell constants, the lattice matching between $MgAl_2O_4$ and Fe is around -0.2 %[28,29].

Bilayers of Fe(20Å)/Pt(30Å) were deposited from elemental Fe and Pt targets by magnetron sputtering in an ultra-high (base pressure $10^{-9} - 10^{-10}$ Torr) vacuum chamber. The Ar gas pressure during sputtering was 2 mTorr and 2.5 mTorr for Fe and Pt, respectively. We used single side polished MgO (100) and $MgAl_2O_4$ (100) substrates with nominal roughness smaller than 5 Å. Substrates were thermally annealed at 550 °C prior to the film deposition. Two identical Fe(20Å)/Pt(30Å) bilayer samples, albeit the substrates, were deposited during the same deposition process. Fe was deposited at 350 °C temperature, while Pt - at room temperature (RT) (*in situ*, after chamber cooled down after Fe deposition). We will refer to these samples as $MgAl_2O_4$/Fe/Pt and MgO/Fe/Pt in the rest of the letter.

X-ray reflectivity (XRR) measurements were performed in order to characterize the interface quality of the samples. The reflectivity curves were fitted using the *GenX* software[31,32]. The recorded experimental XRR curves can be seen in Fig. 2(a). From a qualitative comparison between the two samples, it can be readily observed that Kiessig fringes are more pronounces and persistent at higher 2θ angles for the $MgAl_2O_4$/Fe/Pt samples, hinting towards better layering for it. The individual layer thicknesses d extracted by fitting the XRR curves using *GenX* are: d_{Fe} = 19.4(3) Å and d_{Pt} = 28.0(3) Å for the $MgAl_2O_4$/Fe/Pt sample and d_{Fe} = 18.1(5) Å and d_{Pt} = 28.9(5) Å for the MgO/Fe/Pt sample. It is worth noting here that the $MgAl_2O_4$ substrates are more strongly twinned compared to MgO[33], which means that domains with slightly different crystal orientations are present in these substrates. While it is possible to extract layer roughness values from *GenX* fits of the specular XRR data, the received values are overestimated due to the twinning resulting in off-specular scattering from the samples and do not reflect the qualitative comparison mentioned above. The thickness values, on the other hand, are trustworthy, since the positions of the fringes are clearly distinguishable. To further support this claim as well as for a complete x-ray characterization of the samples, we also performed specular x-ray diffraction (XRD) measurements using a Bede D1 high-resolution x-ray diffractometer, with Cu K_{α_1} radiation, having a wavelength of 1.5406 Å. A comparison between the Fe

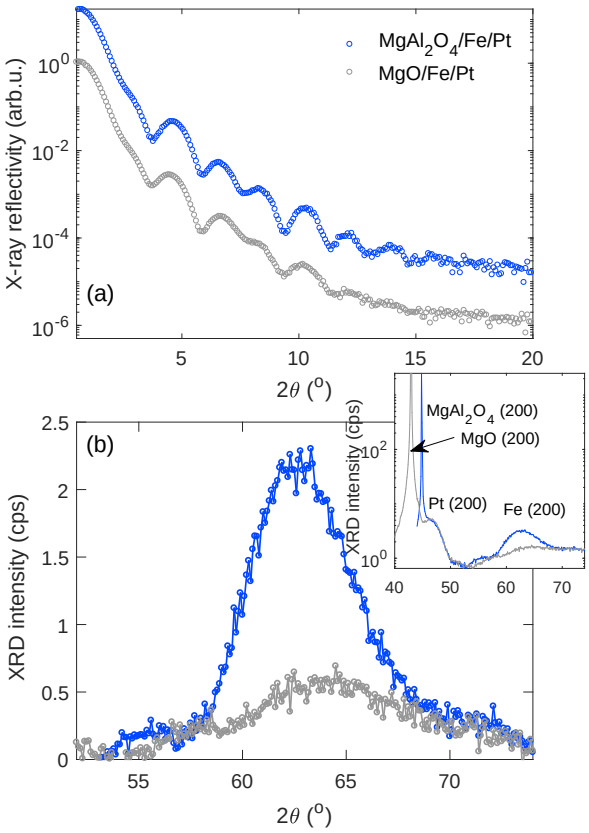

Figure 2. X-ray scattering characterization of $MgAl_2O_4$/Fe/Pt and MgO/Fe/Pt samples (blue and grey, respectively): (a) X-ray reflectivity. The blue curve is shifted upwards for clarity. (b) Fe(200) peaks measured in XRD. Inset: The peak positions for each layer and substrate are indicated in the plot.

diffraction peaks for the two samples is shown in Fig. 2(b). The intensity of the Fe (002) diffraction peak is strongly increased for the $MgAl_2O_4$/Fe/Pt sample. This significant intensity change is an indicator of superior Fe crystal quality, flat interfaces and constant thickness across the whole Fe layer, in the case of the $MgAl_2O_4$/Fe/Pt sample, confirming the observations made by the XRR characterization. We computed the lattice parameters of $MgAl_2O_4$ and MgO substrates from the diffractograms shown in the inset in Fig. 2(b). We obtain 8.08 Å and 8.44 Å along [100] direction (2.86 Å and 2.98 Å along [110] direction, respectively. Additionally, we observe weak Laue oscillations for the $MgAl_2O_4$/Fe/Pt sample on the left-hand-side of the Bragg peak, indicating crystal coherence of the Fe layers. We have to keep in mind that the only difference between the two samples is the substrate material. So most likely the much better lattice matching of $MgAl_2O_4$ to Fe is the cause of the higher Fe layer quality. To the best of our knowledge, such X-rays results have not been reported in other works concerning ultrathin Fe/Pt layers, and if X-ray diffractometry was performed then it was done on much thicker Fe layers in order to obtain sufficient diffraction intensity[34].

THz emission measurements were performed using a femtosecond laser pulse of 800 nm wavelength, 1 nJ energy per pulse, 80 MHz repetition rate and a 10 fs pulse length. The laser spot size on the samples was 20 μm. The THz emission was detected by the means of electro-optical sampling[35] by 10 μm thick ZnTe (110) crystal[5]. Measurements were performed at ambient conditions (RT with no dry gas purging). The samples were saturated by an external in-plane magnetic field (around 30 mT) and illuminated from the backside of the sample, i.e. through the substrate, as shown in Fig. 1(a). In such an experimental configuration, the emitted THz radiation does not propagate through the substrate. Hence, the emitted THz pulse is affected by the metallic bilayer properties only. We measured optical transmission (using UV-Vis spectrometer) of the substrates to correct for the signal reduction due to substrate absorption and scattering of the incident fs-laser pulses in the THz measurements. The light transmission for our $MgAl_2O_4$ and MgO substrates is 26.5 and 13.6 %, respectively. The recorded time-trace signal after the absorption correction is shown in the Figure 3(a). The measured THz radiation is a convolution of a detector response and the beam propagation in the setup.Interestingly, the main pulse has a higher amplitude when emitted from the $MgAl_2O_4$/Fe/Pt than from MgO/Fe/Pt (as compared after the substrate absorption correction). The time-trace was limited to 0.5 ps wide time-windows for both samples and multiplied by the van Hann filter function[36]. Figure 3(a) shows the time trace signals (symbols) and the time-trace signal used for the fast Fourier transform (FFT) after the von Hann filtering.

Despite the large amplitude difference the pulses emitted by the respective samples are similar in length within our measurement accuracy. This could indicate a more efficient spin transfer from Fe to Pt that can be caused by a longer spin diffusion length in Fe. A decrease in spin scattering is well in line with the improved Fe crystalline quality in the $MgAl_2O_4$/Fe/Pt. Better crystallinity causes less spin scattering in the Fe itself but also the transmission through the Fe/Pt interface can increase if the interface is formed with a perfect Fe lattice[8,37].

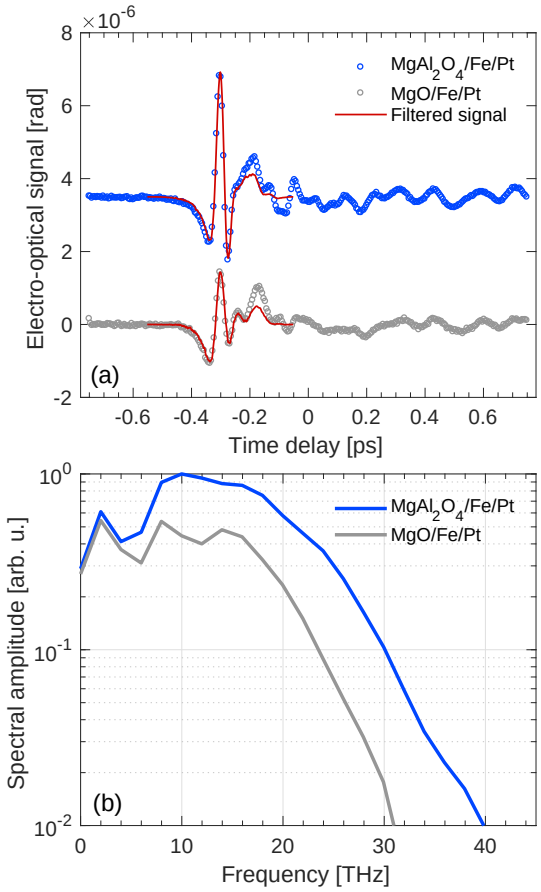

Figure 3. THz emission of the Fe/Pt layers deposited onto MgO and $MgAl_2O_4$ substrates: (a) substrate absorption corrected time-trace of the electro-optical (EO) signals. The curve of the $MgAl_2O_4$/Fe/Pt sample has been shifted upwards for clarity. The sample on $MgAl_2O_4$ substrate has stronger and more persisting signal. Continuous red lines illustrate time traces used for FFT and after multiplication with a von Hann function over the 0.5 ps time window (filtered signal); (b) FFTs of the red line time traces as shown in (a). The spectra are normalized to the peak in amplitude of the $MgAl_2O_4$/Fe/Pt emitter.

The peak-to-peak values of the measured signals of $MgAl_2O_4$/Fe/Pt and MgO/Fe/Pt samples are around 5 μrad and 2 μrad, respectively. The identification of certain features observed in the measured data are the following: (1) The dip at around 5 THz corresponds to the phonon absorption in the ZnTe detector[35]; (2) Contributions from the water in the atmosphere during the measurement appear up until around 10 THz; (3) Additionally, due to a small ZnTe crystal thickness, echoes of the main pulse appear early in the time-domain signal[38]. The echoes would result in the interference fringes in the emission spectra in the frequency domain. Therefore, by reducing the FFT window and applying the filter function, one can reduce the interference fringes in the amplitude spectra as

well as reduce the numerical noise. The spectra were obtained by normalizing the signal in the time-domain to the substrate absorption, as stated above, and performing the FFT over the length of the chosen time window, i.e. 0.5 ps. For comparison, both spectra were then normalized to the peak amplitude of the $MgAl_2O_4$/Fe/Pt spectrum. Figure 3(b) shows the comparison for the two samples. The bandwidth, defined by the frequency at half-maximum, is around 20 THz and 21 THz for MgO/Fe/Pt and $MgAl_2O_4$/Fe/Pt, respectively. So despite the higher emission for $MgAl_2O_4$/Fe/Pt the maximum emission frequency is nearly identical. It can, however, be observed that the MgO/Fe/Pt sample exhibits an almost flat spectrum up to around 16 THz, while $MgAl_2O_4$/Fe/Pt sample has a peak at around 10 THz. The THz amplitude can only be used to compare the magnitude of the spin currents in the respective samples if the resistivity of the films is taken into account[5,9]. To this end, in-plane electrical transport measurements using a standard four-point measurement protocol were performed. For both samples a similar metallic behaviour of the sheet resistance between $T = 300\,\mathrm{K}$ and $T = 10\,\mathrm{K}$ was observed. The sheet resistance is about 8%, larger for the sample grown on $MgAl_2O_4$ ($R_s \approx 105\,\Omega/\square$ at $T = 296\,\mathrm{K}$) compared to the sample grown on MgO ($R_s \approx 97\,\Omega/\square$ at $T = 296\,\mathrm{K}$), excluding the resistivity as primary origin for the substantial difference of the THz amplitude. Remarkably, the residual resistance ratio $\mathrm{RRR} = R_s(298\,\mathrm{K})/R_s(10\,\mathrm{K})$ indicated no substantial difference between the samples' electronic transport properties ($\mathrm{RRR}(MgAl_2O_4/Fe/Pt) \approx 1.35, \mathrm{RRR}(MgO/Fe/Pt) \approx 1.37$).

We have shown that for spintronic THz emitters based on epitaxial Fe an improved crystalline quality of the Fe film can lead to massive enhancement of the THz emission amplitude of up to 250%. The fact that the THz spectrum remains mainly unchanged while the THz amplitude increases indicates that this is caused by decreased spin scattering and better interface transmission as expected for an Fe lattice of superior quality. The emitted bandwidth of 20 THz is comparable to state-of-the-art THz emission sources, namely 5.8 nm thick W/CoFeB/Pt trilayers[5]. Our experiments show that optimization of the layer growth and careful choice of a suitable substrate can be used to improve significantly the characteristics of spintronic THz emitters.

ACKNOWLEDGMENTS

A.C. would like to acknowledge Smålands nation's Anna Maria Lundin's scholarship committee for providing a travel grant. E.T.P., O.G., T.K., G.S. acknowledge financial support by the Deutsche Forschungsgemeinschaft (DFG) in the collaborative research center TRR227, project B02. A.C., A.R., M.P., T.W. and V.K. acknowledge support from the Knut and Alice Wallenberg Foundation project "*Harnessing light and spins through plasmons at the nanoscale*" (No. 2015.0060), the Swedish Research Council (Project No. 2019-03581) and the Swedish Foundation for International Cooperation in Research and Higher Education (Project No. KO2016-6889). V.K. would also like to thank Prof. Peter M. Oppeneer and Prof. Björgvin Hjörvarsson of Uppsala University, Sweden, for fruitful discussions.

REFERENCES

[1] D. M. Mittleman, Journal of Applied Physics **122**, 230901 (2017).
[2] J. Neu and C. A. Schmuttenmaer, Journal of Applied Physics **124**, 231101 (2018).
[3] J. Walowski and M. Münzenberg, Journal of Applied Physics **120**, 140901 (2016).
[4] P. Salén, M. Basini, S. Bonetti, J. Hebling, M. Krasilnikov, A. Y. Nikitin, G. Shamuilov, Z. Tibai, V. Zhaunerchyk, and V. Goryashko, Physics Reports **836-837**, 1 (2019).
[5] T. Seifert, S. Jaiswal, U. Martens, J. Hannegan, L. Braun, P. Maldonado, F. Freimuth, A. Kronenberg, J. Henrizi, I. Radu, E. Beaurepaire, Y. Mokrousov, P. M. Oppeneer, M. Jourdan, G. Jakob, D. Turchinovich, L. M. Hayden, M. Wolf, M. Münzenberg, M. Kläui, and T. Kampfrath, Nature Photon **10**, 483 (2016).
[6] F. Guo, C. Pandey, C. Wang, T. Nie, L. Wen, W. Zhao, J. Miao, L. Wang, and X. Wu, OSA Continuum **3**, 893 (2020).
[7] T. Kampfrath, M. Battiato, P. Maldonado, G. Eilers, J. Nötzold, S. Mährlein, V. Zbarsky, F. Freimuth, Y. Mokrousov, S. Blügel, M. Wolf, I. Radu, P. M. Oppeneer, and M. Münzenberg, Nature Nanotech **8**, 256 (2013).
[8] D. M. Nenno, L. Scheuer, D. Sokoluk, S. Keller, G. Torosyan, A. Brodyanski, J. Lösch, M. Battiato, M. Rahm, R. H. Binder, H. C. Schneider, R. Beigang, and E. T. Papaioannou, Scintific Reports **9**, 13348 (2019).
[9] G. Torosyan, S. Keller, L. Scheuer, R. Beigang, and E. T. Papaioannou, Scientific Reports **8**, 1311 (2018).
[10] Y. Wu, M. Elyasi, X. Qiu, M. Chen, Y. Liu, L. Ke, and H. Yang, Advanced Materials **29**, 1603031 (2017).
[11] D. Yang, J. Liang, C. Zhou, L. Sun, R. Zheng, S. Luo, Y. Wu, and J. Qi, Advanced Optical Materials **4**, 1944 (2016).
[12] H. S. Qiu, K. Kato, K. Hirota, N. Sarukura, M. Yoshimura, and M. Nakajima, Opt. Express **26**, 15247 (2018).
[13] T. Seifert, U. Martens, S. Gunther, M. A. W. Schoen, F. Radu, X. Z. Chen, I. Lucas, R. Ramos, M. H. Aguirre, P. A. Algarabel, A. Anadan, H. S. Karner, J. Walowski, C. Back, M. R. Ibarra, L. Morellan, E. Saitoh, M. Wolf, C. Song, K. Uchida, M. Münzenberg, I. Radu, and T. Kampfrath, SPIN **07**, 1740010 (2017).
[14] R. Schneider, M. Fix, R. Heming, S. Michaelis de Vasconcellos, M. Albrecht, and R. Bratschitsch, ACS Photonics **5**, 3936 (2018).
[15] Y. Ogasawara, Y. Sasaki, S. Iihama, A. Kamimaki, K. Z. Suzuki, and S. Mizukami, Applied Physics Express **13**, 063001 (2020).
[16] Z. Feng, R. Yu, Y. Zhou, H. Lu, W. Tan, H. Deng, Q. Liu, Z. Zhai, L. Zhu, J. Cai, B. Miao, and H. Ding, Advanced Optical Materials **6**, 1800965 (2018).
[17] Z. Jin, S. Zhang, W. Zhu, Q. Li, W. Zhang, Z. Zhang, S. Lou, Y. Dai, X. Lin, G. Ma, and J. Yao, physica status solidi (RRL) Rapid Research Letters **13**, 1900057 (2019).
[18] T. S. Seifert, N. M. Tran, O. Gueckstock, S. M. Rouzegar, L. Nadvornik, S. Jaiswal, G. Jakob, V. V. Temnov, M. Munzenberg, M. Wolf, M. Klaui, and T. Kampfrath, Journal of Physics D: Applied Physics **51**, 364003 (2018).
[19] G. Li, R. Medapalli, R. V. Mikhaylovskiy, F. E. Spada, T. Rasing, E. E. Fullerton, and A. V. Kimel, Phys. Rev. Materials **3**, 084415 (2019).
[20] M. T. Hibberd, D. S. Lake, N. A. B. Johansson, T. Thomson, S. P. Jamison, and D. M. Graham, Applied Physics Letters **114**, 031101 (2019).
[21] D. Kong, X. Wu, B. Wang, T. Nie, M. Xiao, C. Pandey, Y. Gao, L. Wen, W. Zhao, C. Ruan, J. Miao, Y. Li, and L. Wang, Advanced Optical Materials **7**, 1900487 (2019).
[22] E. T. Papaioannou, G. Torosyan, S. Keller, L. Scheuer, M. Battiato, V. K. Mag-Usara, J. L. huillier, M. Tani, and R. Beigang, IEEE Transactions on Magnetics **54**, 1 (2018).
[23] R. I. Herapath, S. M. Hornett, T. S. Seifert, G. Jakob, M. Kläui, J. Bertolotti, T. Kampfrath, and E. Hendry, Applied Physics Letters **114**, 041107 (2019).
[24] R. Adam, G. Chen, D. E. Bürgler, T. Shou, I. Komissarov, S. Heidtfeld, H. Hardtdegen, M. Mikulics, C. M. Schneider, and R. Sobolewski, Applied Physics Letters **114**, 212405 (2019), https://doi.org/10.1063/1.5099201.

[25] J. P. C. Afalla, A. de los Reyes, V. K. Mag-usara, L. P. Lopez, K. Yamamoto, M. Tani, A. S. Somintac, A. A. Salvador, and E. S. Estacio, AIP Advances **7**, 125210 (2017).
[26] I. Ganesh, International Materials Reviews **58**, 63 (2013).
[27] S. M. Hosseini, Physica Status Solidi (b) **245**, 2800 (2008).
[28] J. Koo, H. Sukegawa, and S. Mitani, physica status solidi (RRL) – Rapid Research Letters **8**, 841 (2014).
[29] H. Sukegawa, H. Xiu, T. Ohkubo, T. Furubayashi, T. Niizeki, W. Wang, S. Kasai, S. Mitani, K. Inomata, and K. Hono, Applied Physics Letters **96**, 212505 (2010).
[30] Y. Miura, S. Muramoto, K. Abe, and M. Shirai, Phys. Rev. B **86**, 024426 (2012).
[31] M. Björck and G. Andersson, J. Appl. Crystallography **40**, 1174 (2007).
[32] "*GenX*," (2020), source code available at `https://genx.sourceforge.io/` (retrieved February 2020).
[33] J. Schroeder, A. Ingason, J. Rosén, and J. Birch, Journal of Crystal Growth **420**, 22 (2015).
[34] S. Keller, L. Mihalceanu, M. R. Schweizer, P. Lang, B. Heinz, M. Geilen, T. Brächer, P. Pirro, T. Meyer, A. Conca, D. Karfaridis, G. Vourlias, T. Kehagias, B. Hillebrands, and E. T. Papaioannou, New J. Phys. **20**, 053002 (2018).
[35] A. Leitenstorfer, S. Hunsche, J. Shah, M. C. Nuss, and W. H. Knox, Applied Physics Letters **74**, 1516 (1999).
[36] J. v. Hann and R. D. Ward, *Handbook of climatology* (New York, The Macmillan company; London, Macmillan & co., ltd., 1903).
[37] L. Szolnoki, A. Kiss, B. Dóra, and F. Simon, Scientific Reports **7**, 9949 (2017), number: 1 Publisher: Nature Publishing Group.
[38] E. Beaurepaire, G. M. Turner, S. M. Harrel, M. C. Beard, J.-Y. Bigot, and C. A. Schmuttenmaer, Applied Physics Letters **84**, 3465 (2004).